

Quantum state-resolved reactive scattering of $F+CH_4 \rightarrow HF(v, J) + CH_3$: Nascent $HF(v, J)$ product state distributions

Warren W. Harper, Sergey A. Nizkorodov, and David J. Nesbitt

JILA, National Institute of Standards and Technology and University of Colorado, and Department of Chemistry and Biochemistry, University of Colorado, Boulder, Colorado 80309-0440

(Received 12 April 2000; accepted 1 June 2000)

State-to-state reactive scattering of $F+CH_4 \rightarrow HF(v, J) + CH_3$ is studied using crossed supersonic jets and high-resolution ($\Delta\nu \approx 0.0001 \text{ cm}^{-1}$) IR laser direct absorption techniques. Rovibrational state-resolved HF column-integrated absorption profiles are obtained under single collision conditions and converted to populations via appropriate density-to-flux transformation. Nascent rovibrational distributions in each $HF(v, J)$ state are reported. Summed over all product rotational levels, the nascent vibrational quantum state populations for $HF(v)$ [$(v=3)$ 0.106(3); $(v=2)$ 0.667(14); $(v=1)$ 0.189(27); $(v=0)$ 0.038(78); 2σ error bars] are in agreement with previous flow cell studies by Setser, Heydtmann, and co-workers [Chem. Phys. **94**, 109 (1985)]. At the rotational state level, however, the current studies indicate nascent distributions for $HF(v, J)$ that are significantly hotter than previously reported, ostensibly due to reduced collisional relaxation effects under supersonic jet conditions. Final HF rotational states from $F+CH_4$ are observed near the maximum energetically accessible J values in both the $v=2$ and $v=3$ vibrational manifolds, which provides experimental support for a bent F–H–C transition state structure. © 2000 American Institute of Physics. [S0021-9606(00)00433-5]

I. INTRODUCTION

The study of chemical dynamics in order to understand the detailed mechanics of reactive processes has become increasingly important in chemical physics. In recent years there have been considerable parallel advances in both state-of-the-art experiments^{1–8} and theory,^{9–13} in particular the ability to (i) observe reaction dynamics at the fully quantum state-to-state level, (ii) calculate potential energy surfaces from first principles, and (iii) perform numerically exact quantum scattering calculations on such potential surfaces. It has become increasingly clear that for favorable systems the field has progressed to a point where fully rigorous comparisons between theory and experiment are now feasible. As one benchmark example, the elementary reaction $F+H_2 \rightarrow HF(v, J) + H$ has been a prime focus of attention from experiment, high-level *ab initio* theory, and numerically exact quantum reactive scattering dynamics. Indeed, as noted in a recent review by Manolopoulos,¹⁴ reactive scattering for such “atom+diatom” systems is now theoretically straightforward in all $3N-6=3$ internal degrees of freedom, at least for adiabatic reactions confined to single potential energy surfaces.

By way of contrast, theoretical progress in atom+polyatom systems has remained substantially more recalcitrant, essentially limited by the rapidly increasing internal vibrational degrees of freedom with molecular complexity. What makes these theoretical calculations difficult is the much greater number of *ab initio* points and fitting required to adequately characterize the reactive potential surface, as well as the significantly greater challenge in solving the quantum reactive scattering problem in more than 3 internal degrees of freedom. Nevertheless, this situation is quickly

improving due to rapid advances both in computational chemistry and efficient algorithms for treating reactive scattering in reduced dimensionality.

One important stimulus in the development of such *ab initio* and dynamical efforts is the availability of experimental results for reactive scattering at the fully state-to-state resolved level, such as has recently been achieved for $F+H_2 \rightarrow HF(v, J) + H$ based on direct IR laser spectroscopy on the nascent $HF(v, J)$ product.¹ Natural extensions of this work into more complicated systems with an increasing number of internal dimensions include $F+H_2O$ (atom+triatom), $F+NH_3$ (atom+tetra-atom), and $F+CH_4$ (atom+penta-atom) reactions. The key advantages of such systems are: (i) the high probability of chemical reaction on each collision, (ii) the efficient funneling of chemical exothermicity into HF rotation/vibration, (iii) the presence of only two “heavy” (i.e., nonhydrogenic) atoms, and (iv) the low density of rovibrational energy levels for both products and reactants. In conjunction with the well-studied $F+H_2$ (atom+diatom) system, the above systems form a natural quartet of hydrogen abstraction reactions that should be cleanly accessible with full quantum state resolution under crossed supersonic jet/single collision conditions. Though the most challenging from a theoretical perspective, we have investigated $F+CH_4$ as the second in this series, the results of which form the primary thrust for the work described in this paper. The availability of such quantum state resolved results will hopefully provide the necessary stimulus for both *ab initio* work on high-quality potentials as well as the further development and implementation of new dynamical schemes for calculating reactive scattering on atom+polyatom surfaces.

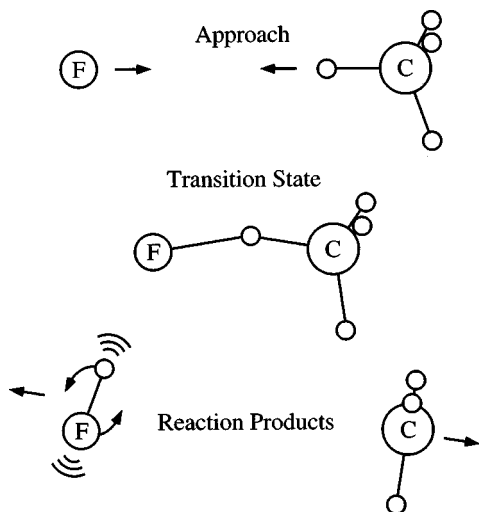


FIG. 1. Simplified view of the $F+CH_4$ hydrogen abstraction reaction. The HF product recoils with a large fraction of the exothermicity in vibrational and rotational energy.

The $F+CH_4 \rightarrow HF+CH_3$ reaction system represents an especially important prototype for highly exothermic hydrogen abstraction reactions of F with hydrocarbons (see Fig. 1). There have been many theoretical investigations of the title reaction at various levels of theory, including several studies of the potential energy surface (PES). At the simplest ‘‘pseudotriatomic’’ level, with the CH_3 group treated as a single ‘‘atom,’’ London–Eyring–Polanyi–Sato (LEPS) surfaces have been developed¹⁵ for the $F+CH_4$ reaction and optimized to reproduce experimental results available at that time. Although significantly below full dimensionality, this LEPS surface has been used to calculate reaction cross sections as a function of collision energy, which have proven successful in reproducing experimental thermal rate constants. More recently, improved surfaces have been developed in full dimensionality^{16,17} including all vibrational coordinates in the CH_3 product. Two of the $F+CH_4$ surfaces are empirical extensions of the *ab initio* $H+CH_4$ potential,^{18,19} while the third version of the surface¹⁶ is obtained from $F+CH_4$ semiempirical calculations (PM3-SRP) modified to reproduce known experimental data. Furthermore, high-level *ab initio* efforts²⁰ have permitted the explicit reaction path and transition state for the title reaction to be determined. The transition state geometry calculated²⁰ at the QCIsd/6-31G(*d,p*) level is found to have a bent structure ($\angle_{F-H-C} = 161.4^\circ$) and an elongated H–F bond length ($r_{F-H} = 1.360 \text{ \AA}$; $r_{C-H} = 1.152 \text{ \AA}$). Most importantly, this bent geometry is indicative of an ‘‘early’’ transition state, corresponding to a H–F distance significantly longer than the equilibrium bond length (0.9168 \AA), specifically falling between the HF classical outer turning points of $v = 4$ (1.318 \AA) and $v = 5$ (1.381 \AA).²¹ Thus, from simple Franck–Condon and impulsive recoil ideas, one expects both substantial vibrational and rotational excitation in the HF product.

A number of experimental investigations have been performed on the $F+CH_4$ reaction, primarily using infrared chemiluminescence and arrested-relaxation techniques. Al-

though the earliest results were strongly influenced by vibrational and rotational relaxation of the product $HF(v,J)$, more recent experiments^{22,23} have made substantial efforts to reduce these collisional effects. The first study under low pressure conditions of the $F+CH_4$ product energy distribution was performed by Nazar and Polanyi,²² which yielded a highly inverted $HF(v,J)$ vibrational distribution [$v = 3,2,1:0.10, 0.69, 0.21$]. The corresponding HF rotational populations roughly resembled a Boltzmann distribution of 300 K, but with increased product density in higher J levels, suggesting a largely, but not completely, relaxed rotational manifold. This work was followed by a detailed FTIR study of HF product state distributions for a series of $F+RH$ reactions by Setser, Heydtmann, and co-workers, including $HF(v=1-3;J)$ rotational distributions from $F+CH_4$.²³ These arrested relaxation HF vibrational distributions for $F+CH_4$ [$v = 3,2,1:0.09(1), 0.73(7), 0.17(2)$] are in good agreement with distributions from the chemiluminescence studies of Nazar and Polanyi;²² however, the possibility of partial rotational relaxation of the nascent HF and secondary reactions²⁴ could again not be ruled out. In analogous F atom abstraction experiments with larger hydrocarbon species,^{23,25-27} the evidence for rotational relaxation was quite dramatic. In particular, the rotational distributions exhibited pronounced shoulders or even double maxima. This behavior was interpreted as arising from strongly J -dependent rotational relaxation dynamics, which prevented high J states from relaxing efficiently due to the large energy gap while allowing the lower J states to become thermalized on the time scale of the detection.

The potential influence of collisions in previous arrested relaxation studies merits further clarification. Specifically, different final quantum states will recoil with different kinetic energies and therefore exhibit different residence times in the detection region. Since very little energy is deposited into the CH_3 fragment, HF quantum states with internal energy close to the exothermicity of the reaction ($v = 3$) will exhibit lower recoil energies than HF with smaller quanta of internal energy ($v = 0,1,2$). These quantum state dependent recoil kinetic energies and free-flight residence times translate into quantum state dependent detection sensitivities for any absorption/emission based experiment. This is the essence of the density-to-flux transformation, which couples the magnitude of an absorption measurement to the residence time of the absorbing chromophore, e.g., an individual quantum state of HF. The density-to-flux transformation becomes negligible with sufficient collisions to cause translational equilibration of the product molecules; however, these collisions unavoidably come with increased opportunity for rotational relaxation. It is therefore especially interesting to revisit this system under single collision conditions, explicitly taking density-to-flux considerations into account.

In this work, the quantum state resolved dynamics of the $F+CH_4 \rightarrow HF(v,J)+CH_3$ reaction have been investigated based on direct absorption of a high resolution IR probe laser under crossed supersonic jet conditions (see Fig. 2). By virtue of the jet expansion geometry, the reagent CH_4 molecules are supersonically cooled into the lowest rotational levels allowed by the nuclear spin statistics prior to reactive scat-

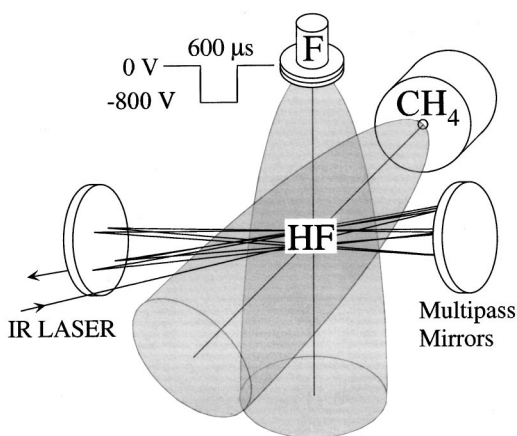


FIG. 2. Schematic of the experimental apparatus. See text for details.

tering. In addition, since these experiments are based on laser absorption rather than spontaneous emission, one can probe the full rovibrational manifold of product HF (i.e., down to $v=0$) for the first time. Most importantly, the low supersonic jet densities and high detection sensitivity allow one to perform the experiment in a regime that cleanly eliminates contributions from collisional relaxation effects and/or secondary reactions.

The organization of the rest of this paper is as follows. In Sec. II, relevant details of the experimental apparatus are provided, followed by a presentation of the nascent HF(v, J) absorbance results in Sec. III. The analysis of these data is discussed in Sec. IV, which addresses Monte Carlo simulation of the density-to-flux transformation and permits extraction of the nascent HF(v, J) rovibrational populations. These results are then discussed in the context of previous work in Sec. V. Section VI summarizes the conclusions.

II. EXPERIMENT

The apparatus used for these reactive scattering experiments has been described in the literature previously;^{1,2} only features specifically relevant to the current study will be summarized here. The crossed jet scattering reactions are performed in a 65 L vacuum chamber pumped by a 10 in. diffusion pump equipped with a liquid nitrogen cold trap and backed with a Roots blower pump. As shown schematically in Fig. 2, two pulsed valves oriented at right angles deliver the F atom and CH₄ reactants, where the distances between the nozzle orifices and the probe laser axis are 5.1 cm and 5.5 cm, respectively. The background pressure is $<5 \times 10^{-6}$ Torr (1 Torr=133.32 Pa) and rises to $<2 \times 10^{-4}$ Torr with the pulsed valves operating at 10 Hz. The HF product molecules are probed in the jet intersection region perpendicular to the plane formed by the two expansion axes, utilizing cw direct infrared laser absorption in a dual beam configuration with two matched InSb detectors. The fluorine atom source used in this experiment^{1,2} is based on a jet-cooled discharge expansion design previously used for high-resolution jet spectroscopy of radicals.²⁸ The source is built around a pulsed solenoid valve body modified² to have a slit aperture (0.60×0.20 cm) sealed by an O-ring. A thin piece of stainless steel, in direct contact with the bottom of

the valve body, is held at ground potential forming the anode and protects the valve body from degradation due to the discharge. A 600 μm plastic spacer separates the anode from the cathode, which consists of two stainless steel slit expansion jaws in electrical contact. The two cathode electrodes form the limiting aperture (400 μm ×0.50 cm) for both the expansion and discharge. This allows the gas between the anode and cathode to rise to the valve backing pressure (35–40 Torr), thereby achieving stable discharge conditions. For the production of fluorine atoms, a 10%:40%:50% (fluorine:neon:argon) mixture expands through the slit in a ~ 2 ms gas pulse, while a -800 V pulse of shorter (500–700 μs) duration on the cathode strikes and maintains the electrical discharge. The transient discharge currents are typically 250–500 mA, stabilized with a 500 Ω ballast resistor. At a 10 Hz repetition rate, this translates into ≈ 1 W average power dissipation, which in vacuum necessitates water cooling to maintain a constant valve temperature of ≈ 25 °C.

The CH₄ reactant is delivered through a piezoelectric pulsed valve based on the design of Proch and Trickl,²⁹ backed with neat methane at pressures between 250–500 Torr. From the measured pulse duration, gas flow, and repetition rate, the effective diameter of the expansion orifice is determined to be 145 ± 5 μm . This is in excellent agreement with the actual 150 μm pinhole diameter, which implies essentially full choke flow expansion conditions. The rotational state distributions of the jet-cooled CH₄ correspond to a temperature of 20 K for each of the three $A(J=0)$, $F(J=1)$, and $E(J=2)$ nuclear spin isomers, as readily determined via direct infrared absorption. The ratio of nuclear spin isomers in the stagnation region is approximately 5:9:2 ($A:F:E$). After supersonic expansion, 85%–90% of the population is cooled into the lowest possible J state for each isomer. Due to high vibrational frequencies, the CH₄ population is nearly entirely in the ground vibrational state; even at room temperature stagnation conditions, there is only about 0.1% and 0.6% population in the bending ν_2 and ν_4 vibrational modes, respectively, with vanishingly small contributions in either of the ν_1 or ν_3 stretching modes.

The infrared radiation is produced by a color center laser, pumped by the red lines of an amplitude stabilized krypton ion laser and modified³⁰ for continuous single mode scanning up to 0.8 cm^{-1} intervals with 2 MHz resolution. The laser beam is multipassed 18 times through the vacuum chamber in a Herriott cell configuration to enhance detection sensitivity. The multipassed IR laser beam forms an elliptical pattern³¹ approximately 8 mm high by 5 mm wide centered at the intersection region. HF($\Delta v=1$) rovibrational transitional frequencies are calculated using the improved rotational constants of Ram *et al.*,³² where residual errors are well within the experimental Doppler width. Time-dependent absorbance signals are recorded with a transient digitizer and transferred to a computer for analysis on a pulse-to-pulse basis. Dual software gates (100 μs width) are used to record background and transient absorption signals, as well as exclude very weak delayed signals due to HF molecules formed by pulsed F atom reactions on the chamber walls. Data collection is therefore restricted to the middle 400 μs

of the 500 μs CH_4 gas pulse, with the gates turned off before the HF molecules have time to travel back into the detection region. The absolute absorbance is recorded as the frequency of the laser is scanned in 3–5 MHz increments over the entire Doppler profile for each transition studied. Etalon fringes are recorded simultaneously with the Doppler profile to provide relative frequency calibration, while a phase locked loop travelling Michelson interferometer³³ is used with a polarization stabilized HeNe laser to determine the absolute IR laser frequency. Residual power fluctuations in the IR light are monitored on the IR reference laser, which are used with fast servoloop feedback electronics to control the amplitude of the krypton ion pump laser.

Conditions have been chosen to make the effects of secondary reactions negligible by lowering the gas densities in the jet intersection region. The reaction probability (P) can be estimated from $P = \sigma NL$, where σ is the reaction cross section ($\approx 5 \times 10^{-16} \text{ cm}^2$, inferred from the room temperature rate constant),³⁴ N is the density, and L is the path length for the reactants. The total F atom density from the discharge source is estimated to be $7 \times 10^{11} \text{ cm}^{-3}$ (in $1.5 \times 10^{14} \text{ cm}^{-3}$ of carrier gas) while the density of CH_4 is about $7 \times 10^{12} \text{ cm}^{-3}$, each evaluated at the laser intersection region. Based on an effective path length of 5 cm, the reaction probability for each F atom is $< 2\%$, thus reducing the probability of sequential reactions to negligible levels ($< 0.02\%$). On the $< 40 \mu\text{s}$ time scale that individual HF molecules arrive and fly through the detection region, vibrational or rotational state changing effects due to spontaneous emission can be completely neglected. Furthermore, probe laser power levels ($< 60 \mu\text{W}$) are more than an order of magnitude below saturation levels so as to insignificantly perturb the nascent $\text{HF}(v, J)$ populations. Under such expansion conditions, the signal to noise ratio for the strongest absorption feature is $S/N \approx 30$ per pulse, with a rms absorbance noise floor of 7×10^{-5} in a 20 kHz detection bandwidth. Since the *integrated* absorbance measurement values reflect integration over ≈ 1000 points across the Doppler profile, the resulting S/N ratio for the product column integrated densities is further enhanced by ≈ 15 - to 20-fold.

III. RESULTS

High-resolution IR absorption Doppler profiles have been collected for all fundamental and hot band ($\Delta v = +1$) HF rovibrational transitions accessible within the tuning range of the F-center laser (2.5–3.3 μm). A summary of the full network of $\text{HF}(v', J') \leftarrow \text{HF}(v'', J'')$ transitions probed is shown in Fig. 3, and the energetics are presented in Fig. 4, where ΔE_{com} is the collision energy for a perpendicular collision geometry and ΔE_{rxn} is the 31.84(3) kcal/mol exothermicity of the reaction. It is worth noting that these profiles are obtained on 50 populated rovibrational levels (up to the $v \leq 3$ energetically accessible manifold) connected by 45 *P*-branch and 29 *R*-branch transitions. As a test of internal consistency, the number of independent measurements exceeds the number of inferred quantum state populations by ≈ 1.5 -fold. The Doppler profiles for each transition are recorded multiple times (typically 2–4) to enhance statistics,

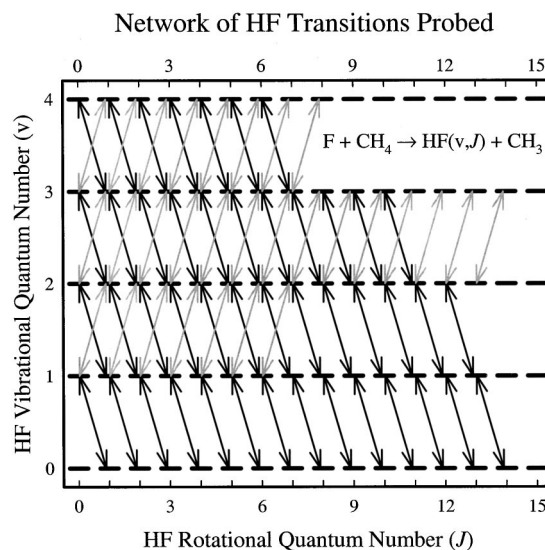


FIG. 3. Network of HF absorption/stimulated emission transitions probed. For the $v=3, 2$ vibrational levels, we probe J up to the energetic limit, while for $v=1, 0$ we probe all levels within the tuning range of our F-center laser. The high level of redundancy (~ 1.5 -fold) in the measurements enhances the statistics of our population measurements.

scanned over 0.2 cm^{-1} (≥ 8 times the typical FWHM), and integrated over all frequency steps to obtain integrated absorbances in absolute units. Finally, each Doppler profile is also scanned with and without the CH_4 valve operating to correct for weak background absorbance (typically 0%–10% of the peak signals) due to trace HF impurities present in the F atom source. The development of such an extensive data set necessarily reflects data collection over many weeks of experimentation. Therefore, both to improve reliability on individual lines as well as to combine data from different days, a reference Doppler profile [$v=4 \leftarrow 3; R(0)$] is recorded after every third transition and used to correct for slow variations in the pulsed F-atom/ CH_4 densities in the jet intersection region. We find that this procedure works extremely well to improve the quality and reproducibility of the data set.

Selected HF Doppler profiles for *P*- and *R*-branch transitions are shown in Fig. 5 and Fig. 6, respectively, and immediately indicate several points worth noting. First, the data testify to the high sensitivity of the measurements, typically with $S/N \approx 3$ –30 for absorbances at line center, and improved to $S/N \approx 50$ –500 by integration over the Doppler profile. Second, the line shapes are both positive and negative, i.e., corresponding to either absorption or stimulated emission signals. This simply reflects the fact that an absorption measurement necessarily samples population differences between the upper and lower probe states. For example, all of the $v=4 \leftarrow 3$ data reflect pure absorption signals due to insufficient reaction exothermicity to populate rotational states in the $\text{HF}(v=4, J)$ manifold. Conversely, the $\text{F} + \text{CH}_4$ reaction generates a strong population inversion between $v=2$ and $v=1$, which results in primarily stimulated emission signals on each of the $v=2 \leftarrow 1$ probe transitions. Third, there is considerable Doppler structure evident in these profiles, where the absorbance shifts from negative to positive

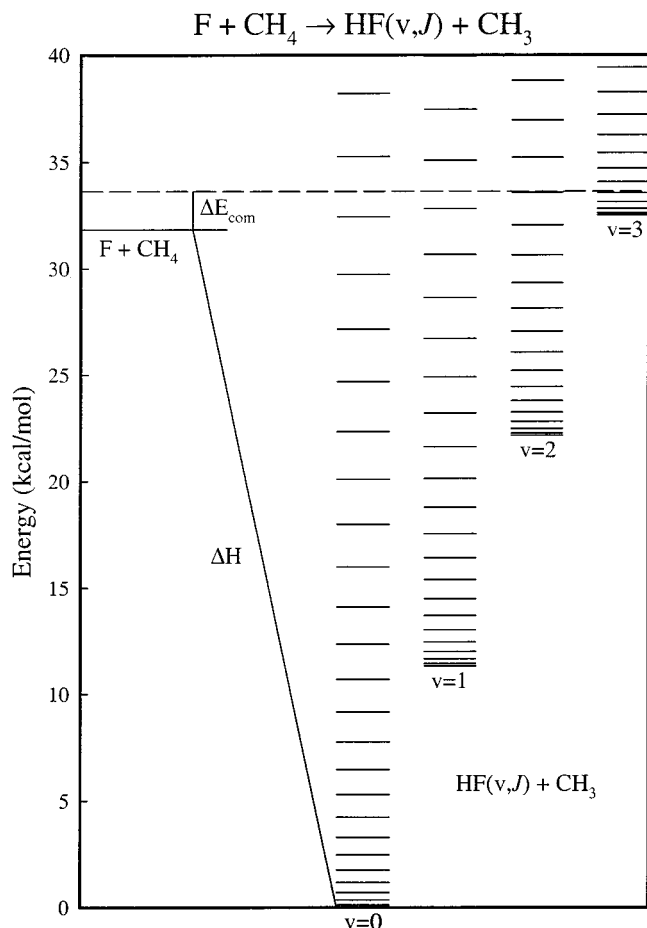


FIG. 4. Energetics of the $F+CH_4$ reaction. The dashed line shows the total exothermicity of the reaction, including the contributions from ΔH and the center-of-mass collision energy ΔE_{com} . The $v=3$ manifold is accessible up to $J=4$ for a perpendicular collision geometry, and slightly higher for obtuse collision geometries. Not shown is the energy contribution ($\Delta E_{so} = 1.15$ kcal/mol) from the spin-orbit excited fluorine, which would allow $v=3$, $J=6$ to be populated.

for small and large Doppler detunings, respectively [e.g., $v=3 \leftarrow 2$; $P(2)$]. In addition to these velocity dependent population inversions between different rovibrational manifolds, line widths are also observed to change depending on the HF quantum state. This is strong evidence that even the translational energy distribution is not relaxed, providing additional confirmation that the rotational and vibrational distributions are indeed nascent. As described elsewhere in more detail, these Doppler profiles can be used to extract partial information on the differential cross sections for reactive scattering into a final quantum state.³⁵

The integrated absorbances are converted to column-integrated densities according to

$$\int A(\nu) d\nu = \frac{8\pi^3 \nu_0 |m| \mu^2}{3hc} \left[\frac{\int [HF(v'', J'')] dl}{(2J''+1)} - \frac{\int [HF(v', J')] dl}{(2J'+1)} \right]. \quad (1)$$

In this expression, $A(\nu)$ is the frequency dependent absorption coefficient integrated over the entire Doppler profile, ν_0 is the center transition frequency, and m is the rotational

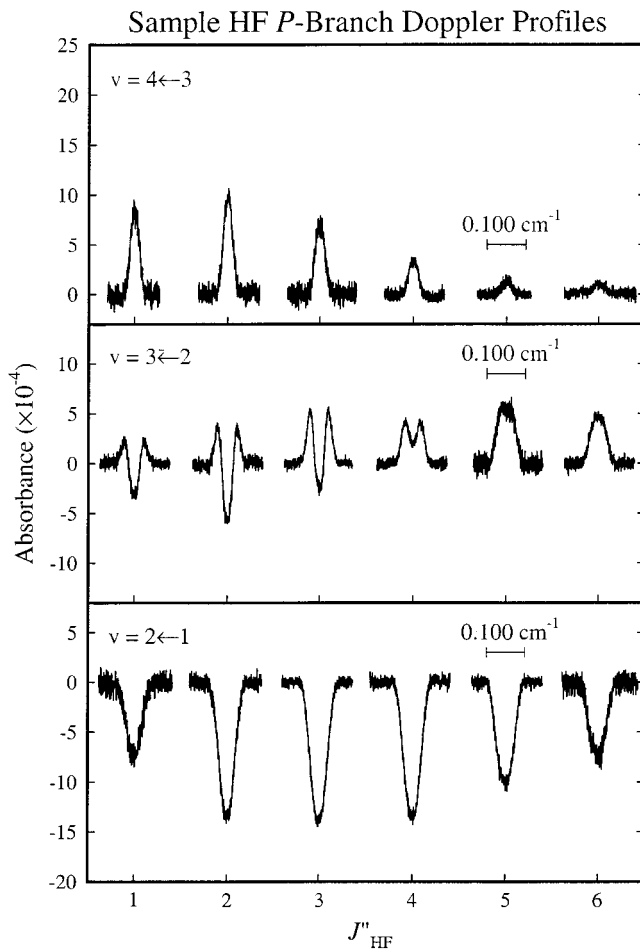


FIG. 5. Representative HF(v, J) P -branch Doppler profiles. Doppler profiles consist of pure absorption ($v''=3$ manifold), stimulated emission ($v''=1$), or a combination of the two ($v''=2$).

numbering index ($m = -J''$ for P -branch transitions, $m = J'' + 1$ for R -branch transitions). In Eq. (1), μ is the HF rovibrational transition dipole moment derived from extensive studies by Setser and Stwalley which correctly include rotational Herman Wallis effects.^{36,37} As noted above, the signals reflect population differences in the upper and lower states, which are mirrored by the absorption and stimulated emission terms in the right-hand side of Eq. (1). Specifically, the integrals on the right-hand side of Eq. (1) yield HF(v, J) column-integrated densities over the laser beam through the detection region, which in turn are determined by simultaneously least squares fitting the integrated absorbance data for the full set of lines to equation Eq. (1). The high redundancy of the line measurements permits the least squares goodness of fit parameter to be used with the variance-covariance matrix to estimate standard errors associated with each of these column-integrated densities.

IV. ANALYSIS

In any direct absorption detection experiment (and common to most laser based probe techniques), one directly measures the product densities, whereas the reaction cross section is rigorously defined in terms of product fluxes. In general, these two quantities are not identical and differ by

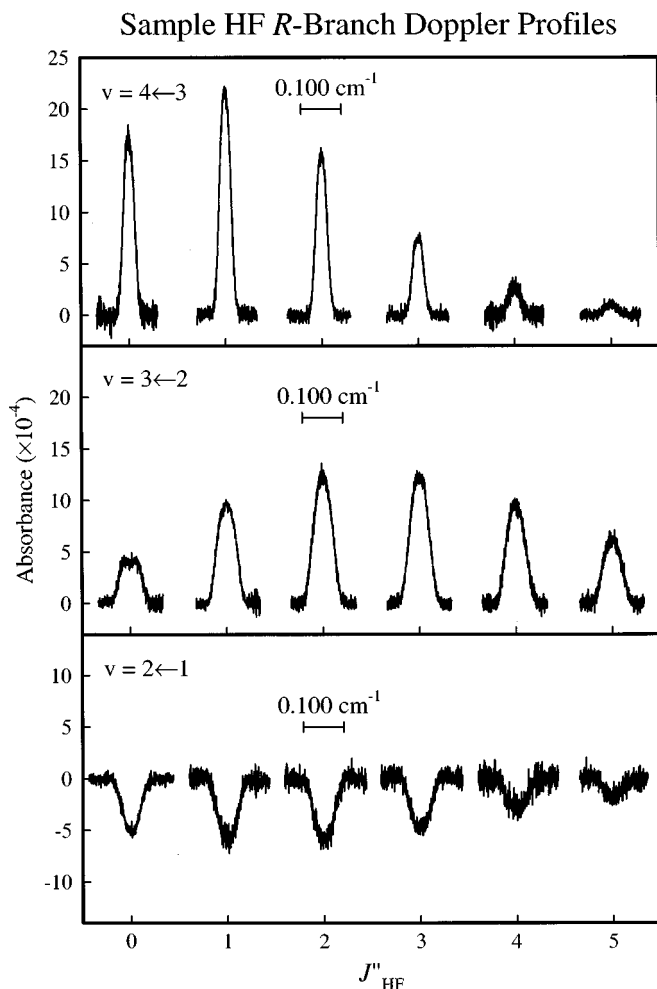


FIG. 6. Representative HF(v, J) R-branch Doppler profiles. Doppler profiles primarily reflect absorption ($v''=3$) or stimulated emission ($v''=1$). However, for $v=2, J=0$ a small amount of stimulated emission can be seen in center of the profile. Although not immediately visible, there are also small stimulated emission contributions in other transitions originating from the $v''=2$ vibrational manifold. Note the differences in the linewidths of various transitions as a function of the HF quantum state.

the density-to-flux transformation, which depends on several factors including the magnitude of the energy release and thus the final quantum state of the products. Therefore, in order to facilitate rigorous comparison with theoretical and other experimental results, the laboratory frame column-integrated densities obtained in Sec. III must be properly transformed into molecular fluxes in the center-of-mass frame. For heavy+light-light systems such as $F+H_2$, the kinematics are quite favorable such that the desired HF fluxes are closely proportional to the experimentally observed column-integrated densities. However, the HF recoil effects are much larger for $F+CH_4$, which make this transformation much more relevant to take into account, as treated below.

A. Monte Carlo simulation of density-to-flux transformation

To address the issue of detection sensitivity on the residence time, detailed Monte Carlo simulations have been performed to incorporate the density-to-flux transformation as a function of E_{recoil} , or equivalently HF(v, J) quantum state.

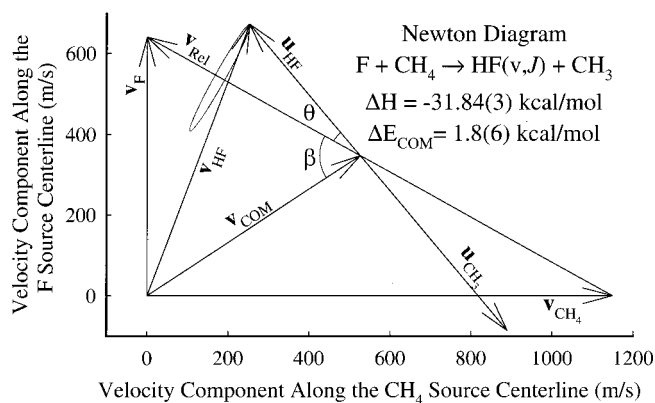


FIG. 7. Newton diagram for the $F+CH_4$ reaction with perpendicular collision geometry. The vectors \mathbf{v} represent lab frame velocities, while the vectors \mathbf{u} represent center-of-mass frame velocities. The center-of-mass scattering angle is given by θ and the azimuthal scattering angle ϕ (averaged over in all of our calculations) traces a circle perpendicular and centered on \mathbf{v}_{rel} . HF and CH_3 recoil from each other with velocities that are determined from conservation of momentum and the internal energy for both molecules.

The Newton diagram in Fig. 7 shows an idealized geometry for reactive scattering of $F+CH_4$, where $\mathbf{v}_F(\mathbf{u}_F)$ and $\mathbf{v}_{CH_4}(\mathbf{u}_{CH_4})$ denote the F atom and CH_4 velocity vectors in the laboratory and center-of-mass frame (COM), respectively. The centerline magnitudes of \mathbf{v}_F and \mathbf{v}_{CH_4} are 641 and 1150 m/s, respectively, as calculated using standard supersonic jet formulas and confirmed by direct time of flight measurements. This idealized perpendicular geometry corresponds to a collision energy of $E_{\text{com}}=1.8(6)$ kcal/mol, where the width is dominated by angular averaging over the finite distribution of angles between \mathbf{v}_F and \mathbf{v}_{CH_4} (see Ref. 8 for more details). After the reaction, HF is emitted in the center-of-mass frame at some angle θ with respect to \mathbf{v}_{rel} ; for unaligned reagents, one integrates over the azimuthal angle ϕ (i.e., the cone about \mathbf{v}_{rel} , to yield differential cross sections ($d\sigma/d\Omega$) for reactive scattering into a given final state. The product molecules recoil in the COM frame with final velocity vectors \mathbf{u}_{HF} and \mathbf{u}_{CH_3} ; the product HF is then probed by direct IR absorption where the Doppler shifts are easily calculated from the lab frame velocity component of \mathbf{v}_{HF} (i.e., $\mathbf{u}_{\text{HF}}+\mathbf{v}_{\text{COM}}$) parallel to the probe laser axis. The relevant weighting of these events (i.e., the density-to-flux transformation) is proportional to how long the product stays in the laser beam, which is inversely related to v_{\perp} , i.e., the component of \mathbf{v}_{HF} perpendicular to the probe axis.

In the calculations, random points are chosen inside of a small sampling volume at the jet intersection. The collision energy along with the exothermicity of the reaction ($\Delta H = -31.84$ kcal/mol) provides the total energy available for partitioning among the two product molecules. The relevant quantity is therefore the recoil energy in the center-of-mass frame, i.e.,

$$E_{\text{recoil}} = E_{\text{com}} - \Delta H - E_{\text{HF}} - E_{\text{CH}_3}, \quad (2)$$

where E_{HF} and E_{CH_3} represent the amount of total energy left in internal quantum states of the product. Once this recoil energy is specified, (*vide infra*), the collision energetics and

product speeds can be readily calculated from conservation of energy and momentum. The HF product velocities are then distributed in center-of-mass angle θ according to the differential cross section, $d\sigma/d\Omega$, which permits the calculation of the desired flux-to-density conversion factor ($\propto v_{\perp}$) for a given value of θ and averaged over $\phi=0-2\pi$.

For a known initial collision energy, reaction exothermicity, and final HF(v, J) quantum state, the choice of E_{recoil} depends only on the internal energy in the CH₃ subunit. Fortunately, as shown by Sugawara *et al.*,³⁸ the internal energy of CH₃ is quite small compared to the exothermicity of the reaction. Their study reports a relatively cold vibrational distribution in the ν_2 (umbrella bending 606 cm⁻¹) mode of CH₃, with fractional populations of 0.67($\nu_2=0$), 0.24($\nu_2=1$), and 0.09($\nu_2=2$) (Ref. 38) (corresponding to $T_{\text{vib}} \approx 1000$ K). Furthermore, the nascent rotational energy distribution appears to be approximately Boltzmann with a corresponding temperature of 280(40) K. By way of confirmation, we have also observed CH₃ infrared transitions based on the ν_3 CH stretch fundamental, albeit at tenfold higher CH₄ backing pressures necessary to enhance detection sensitivity. While no longer purely in the single collision regime under these higher pressure conditions, the CH₃ populations are at least qualitatively consistent with the cold distributions obtained by Sugawara *et al.* Based on these previous CH₃ rovibrational distributions, the average internal energy $\langle E_{\text{CH}_3} \rangle$ is ≈ 1.61 kcal/mol, which represents a small fraction of the 31.84 kcal/mol reaction exothermicity. However, even this average energy represents an overestimate for the highest HF(v, J) states, which are populated up to the energetic limit. Thus, as the simplest model consistent with experimental results, E_{CH_3} is assumed to be linearly anticorrelated with E_{HF} , i.e.,

$$\langle E_{\text{CH}_3} \rangle = 4.978 - 0.150 \langle E_{\text{HF}} \rangle, \quad (3)$$

with the proportionality constants chosen to make E_{CH_3} vanish at the energetic limit and $\langle E_{\text{CH}_3} \rangle = 1.61$ kcal/mol when averaged over the nascent distribution of HF(v, J) product states. It is worth noting that the reported HF(v, J) populations are quite insensitive to various modelings of the CH₃ energy distribution, up to and including the complete neglect of CH₃ internal energy. The essential reason for this insensitivity is that the 1.61 kcal/mol average internal energy of CH₃ is perturbatively small ($\approx 5\%$) compared to the overall 31.84 kcal/mol exothermicity of the reaction.

B. Nascent HF(v, J) populations

In order to convert the measured column-integrated densities into state-resolved nascent populations, one needs the density-to-flux conversion factor, $f(v, J)$, for each final HF(v, J) state. These $f(v, J)$ can be obtained from the Monte Carlo simulations described above by averaging over all center-of-mass scattering angles θ , and weighting the results by the differential cross sections. Quantitative extraction of the nascent HF(v, J) populations from any absorption/emission experiment therefore requires some prior knowledge of the state-resolved differential scattering cross sections of the product molecules. Toward this goal, we have

used high resolution Dopplerimetry to obtain such information for a selection of rovibrational product states in the HF($v=1,2$) manifold, as described elsewhere in more detail.³⁵ However, the product state distributions are relatively insensitive to the form of these differential scattering cross sections, primarily because $f(v, J)$ depends on v_{\perp} in the laboratory frame, which is typically dominated by the forward motion of the center-of-mass. Thus, based on differential cross sections obtained from high resolution Dopplerimetry for a series of J states in HF($v=1,2$), we approximate the differential cross sections as $d\sigma/d\Omega \propto |\cos(\theta)|$, which roughly corresponds to forward/backward peaked distributions in the center-of-mass frame. This is also consistent with a more complete Dopplerimetry analysis of HF($v=1,2$).³⁵ Unfortunately, Doppler information is not available for differential scattering into the HF($v=3$) manifold, since the recoil energies are now too small to contribute significantly to the experimental linewidths. However, the HF($v=3$) populations also prove quite insensitive to the choice of scattering model; specifically, forward, sideways, and isotropic scattering models yield identical results within experimental uncertainties (5%). We therefore have assumed an isotropic distribution for HF($v=3$), but note that the inferred populations would increase slightly ($\approx 20\%$) in the dynamically improbable limit of pure back scattering.

Based on these approximate forms for the differential scattering cross sections, an average residence time may be calculated for a given E_{recoil} by the Monte Carlo methods. The density-to-flux transformation factor $f(v, J)$ is proportional to the inverse of this residence time, which, when multiplied by the column-integrated density, results in a scattered flux (or population). E_{recoil} is obtained by energy conservation from the known reaction exothermicity, center-of-mass collision energy, and internal energies in the HF(v, J) and CH₃ products. Since the amount of energy in the CH₃ product is only a small fraction of the reaction exothermicity, the extracted HF(v, J) rovibrational populations are insensitive to the CH₃ internal energy distribution. Indeed, complete neglect of CH₃ internal energy would result in negligible differences ($< 2\%$) in the normalized populations of $v=0,1,2$ and only a small decrease in the $v=3$ populations ($< 10\%$).

Table I reports both (i) $f(v, J)$, density-to-flux transformation factors, and (ii) nascent populations for each HF(v, J) rovibrational level, based on $d\sigma/d\Omega \propto |\cos(\theta)|$ for $v=0,1,2$ and isotropic scattering for $v=3$. The rotationally resolved populations are depicted graphically in Fig. 8. The 1σ confidence interval for the reported populations have been propagated from the variance/covariance matrices obtained from the least squares fit and given by the error bars in Fig. 8 for each rovibrational level and listed in Table I. The corresponding HF(v) populations, summed over all J for a given vibrational manifold, have been plotted in Fig. 9 for the present data as well as the previous studies of Polanyi *et al.*, Ref. 22 and Setser *et al.*, Ref. 23. For $v=3$ populations, the calculated uncertainties are quite small but increase systematically for the lower ($v=0-2$) vibrational levels. This is because absorption measurements reflect population differences between upper/lower states, which implies the

TABLE I. Nascent HF(v, J) rovibrational distributions and state specific density-to-flux transformation constants. The transformation constants result from treating HF($v=0,1,2$) with backward ($d\sigma/d\Omega \propto |\cos(\theta)|$) scattering and HF($v=3$) with isotropic ($d\sigma/d\Omega = \text{constant}$) scattering. Numbers in parenthesis are 1σ errors.

J_{HF}	$v_{\text{HF}}=3$		$v_{\text{HF}}=2$		$v_{\text{HF}}=1$		$v_{\text{HF}}=0$	
	Frac. Pop.	DF Const.						
0	1.58(1)	0.565	4.5(1)	1.313	0.5(2)	1.706		2.024
1	3.25(5)	0.570	10.5(2)	1.308	1.6(4)	1.702	2.3(22)	2.021
2	2.87(6)	0.580	12.5(2)	1.299	1.2(4)	1.695	1.8(13)	2.015
3	1.85(5)	0.593	12.1(2)	1.285	1.1(4)	1.684	-1.1(12)	2.006
4	0.63(6)	0.610	9.9(1)	1.266	1.5(4)	1.670	-1.5(9)	1.994
5	0.25(7)	0.629	6.8(2)	1.241	1.8(3)	1.561	-0.2(10)	1.979
6	0.16(7)	0.652	4.1(2)	1.211	1.4(4)	1.629	0.5(9)	1.960
7	0.00 ^a	0.677	2.6(2)	1.174	1.6(4)	1.603	0.8(8)	1.938
8			1.6(1)	1.131	2.5(4)	1.572	-0.0(9)	1.913
9			1.2(1)	1.080	1.5(4)	1.536	1.6(9)	1.884
10			0.4(1)	1.020	1.6(4)	1.495	-0.2(8)	1.851
11			0.3(1)	0.949	0.9(3)	1.448	0.1(8)	1.813
12			0.2(3)	0.864	1.0(3)	1.396	-0.6(7)	1.772
13			0.0(3)	0.758	0.7(5)	1.336	0.3(7)	1.725
14			0.0(3)	0.624		1.267	0.2(9)	1.673
ΣJ	10.6(1)		66.7(7)		18.9(14)		3.8(40)	

^aParameter constrained to be positive.

least uncertainty for the highest HF($v=3, J$) vibrational manifold. As a direct corollary, uncertainties accumulate down the vibrational manifold, culminating in the largest uncertainties in the HF($v=0, J$) level, where rotational populations nearly vanish within experimental error bars (1σ). Although a more detailed discussion of these distributions is reserved until Sec. V, several comments are briefly worth noting at this stage. First of all, the $f(v, J)$ values range over 3.5-fold, illustrating the importance of a density-to-flux analysis in any experiment with unequilibrated translational degrees of freedom. Second, the nascent HF vibrational populations summed over rotational states are in excellent agreement with the arrested relaxation studies by both Polanyi *et al.* and Setser *et al.* Finally, at the rotationally state-resolved level, the distributions from this study are distinctly hotter than previously obtained from early IR chemiluminescence studies.

V. DISCUSSION

The HF(v, J) rovibrational distributions from $\text{F} + \text{CH}_4 \rightarrow \text{HF}(v, J) + \text{CH}_3$ have been previously characterized in two arrested relaxation studies.^{22,23} However, partial rotational relaxation and secondary reactions²⁴ of the products could not be ruled out, and the population in the $v=0$ manifold could not be determined. The combined efforts²³ of the Setser and Heydtmann groups (SH) reported modest agreement ($v=3:0.09$, $v=2:0.73$, $v=1:0.17$) between arrested relaxation and flow reactor experiments, which were in good agreement with the earlier work of Polanyi²² ($v=3:0.10$, $v=2:0.69$, $v=1:0.21$). Surprisal analysis³⁹ estimates of the HF($v=0$) population predicted this to be negligibly small²³ compared to the other vibrational levels. Indeed, the present IR absorption measurements (which probe $v=0$ directly) now confirm this prediction for the first time; the total branching into HF($v=0$) is $3.8 \pm 4.0\%$, with 1σ

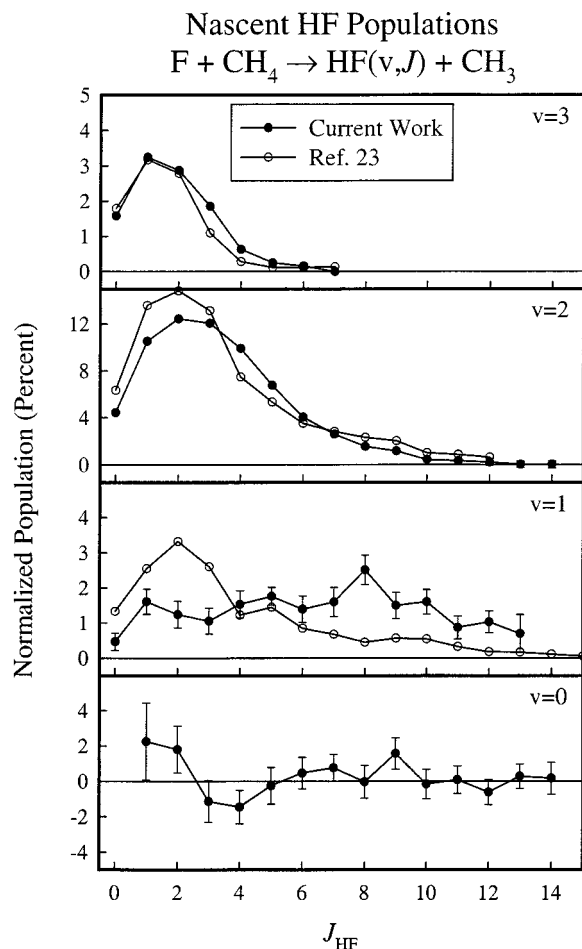


FIG. 8. Nascent HF(v, J) fractional product populations. The filled circles are the results of the current work after density-to-flux transformation (with 1σ error bars), and the open circles are the results from Ref. 23 (SH). The rotational distributions exhibit a consistent broadening as the vibrational energy is decreased. Note the differences particularly in the $v=1$ manifold between current and previous work (Ref. 23).

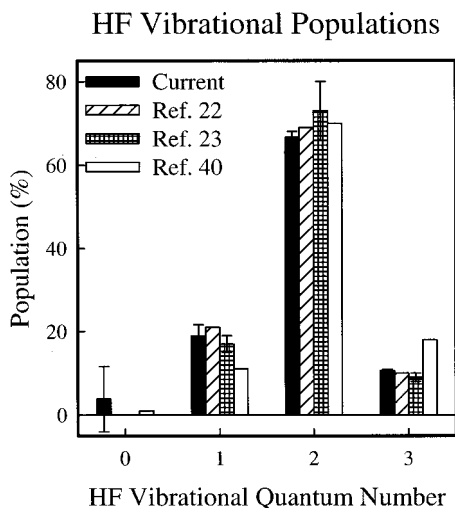


FIG. 9. Comparison of HF vibrational populations from Ref. 22 (Polanyi), Ref. 23 (SH), Ref. 40 (Gonzalez), and the current work. The previous work is based on IR emission, hence the population in $v=0$ could not be determined directly. Populations from Ref. 22 are given without error bars.

error bars as large as the population. Taken one step further, we have recalculated a vibrational surprisal plot based on data in all HF($v=3,2,1,0$) manifolds; the results are displayed and compared to the results of SH (Ref. 23) and theoretical predictions by Gonzalez⁴⁰ in Fig. 10. The vibrational distributions of HF are indeed remarkably well represented by a single surprisal parameter, which corresponds to a single constraint superimposed on a statistical (prior) distribution.

As shown in Fig. 9, excellent agreement exists between past and present studies of HF vibrational energy distributions [$(v=3)$ 0.106(3); $(v=2)$ 0.667(14); $(v=1)$ 0.189(27); $(v=0)$ 0.038(78); (2σ)]. However, the earlier rotational distributions appear to be somewhat relaxed in each vibrational level when compared with the present work (Fig. 8). First of all, the present rotational distributions are consistently broader in all vibrational levels than previously reported. Second, the most populated J states occur at

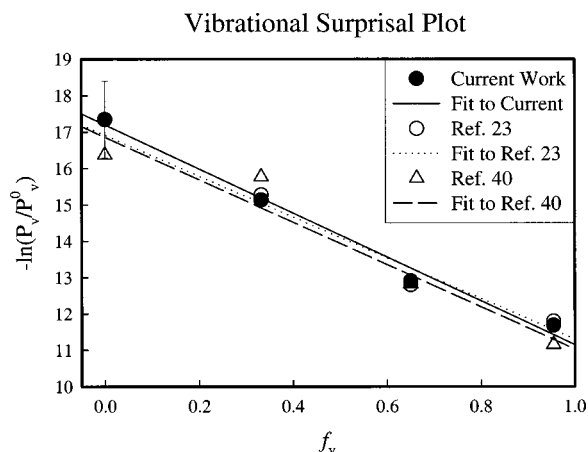


FIG. 10. Vibrational surprisal analysis comparing the current results to that of Ref. 23 (SH, experiment) and Ref. 40 (Gonzalez, theory). The vibrational distribution is well characterized by a single constraint superimposed on a statistical (prior) distribution.

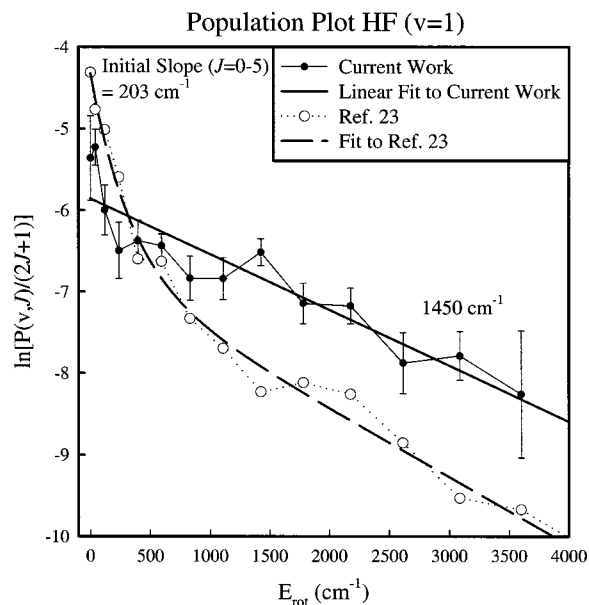


FIG. 11. Boltzmann plot for the current HF($v=1$) populations and those of SH. The current work is characterized by a reciprocal slope of $\approx 1450 \text{ cm}^{-1}$. The previous work indicates a room temperature initial slope at low J , while the high J data gives slopes that approach our value. A 300 K equilibrium distribution would correspond to a reciprocal slope of 208 cm^{-1} .

higher rotational levels. These effects are particularly evident in the $v=1$ vibrational manifold in Fig. 8, where the previous (SH) distribution peaks early at $J=2$, while the present distribution exhibits a much broader peak around $J \approx 8$. Alternatively, Fig. 11 compares data from the current and previous studies in Boltzmann plots for the rotational levels of HF($v=1$), where a straight line would correspond to a uniform rotational temperature. In this plot, the SH data exhibit a reciprocal slope of $\approx 200 \text{ cm}^{-1}$ (i.e., $\approx kT$ at room temperature) for the lower J levels, while the higher J data approaches a reciprocal slope of $\approx 1200 \text{ cm}^{-1}$. By way of comparison, the current data show much less curvature at low J values, and are adequately represented over all J by a reciprocal slope of $\approx 1450 \text{ cm}^{-1}$. This behavior would be qualitatively consistent with partial thermal equilibration in the previous work for low J rotational levels, where the smaller rotational energy spacings make HF more susceptible to collisional energy transfer effects.

As mentioned above, the previous studies have neglected any effects due to density-to-flux transformations; the connection between this and rotational relaxation are intimately related. By neglecting this transformation, previous studies are implicitly assuming translational equilibrium between product states, though without any change in HF(v,J). This assumption is based on the reasonable expectation that translational degrees of freedom relax on a faster time scale than rotation and, in turn, much faster than vibration. Nevertheless, such equilibration of translational energy distributions requires some collisions, which also necessarily introduces the possibility of rotational relaxation effects. It is therefore interesting to note that the agreement between current and previous vibrational populations is significantly improved when integrated over all J rotational levels. One self-consistent interpretation would be that the previous experi-

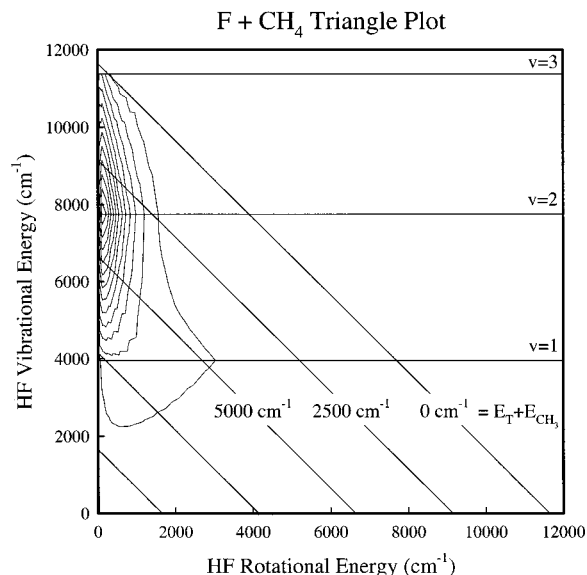


FIG. 12. Triangle contour plot for the HF product energy distribution. The diagonal lines form an axis that gives the quantity $E_T + E_{\text{CH}_3}$. We estimate that 80%–85% of this energy is due to translational energy (E_T). The HF product is in a nonstatistical distribution with a large fraction of the exothermicity going into vibrational energy.

ments were performed under conditions that permit nascent vibrational distributions to be obtained, although with partial rotational relaxation in the collisionally more susceptible lower J levels.

In the spirit of the early dynamical analysis of Polanyi and co-workers, a triangle plot (see Fig. 12) shows how the $\text{F} + \text{CH}_4$ reaction exothermicity is distributed into the HF product molecules. Since there are more than three atoms, this triangle plot has the added feature that the diagonal axis represents not just translational energy (E_T), but a sum of E_T and CH_3 internal energy (E_{CH_3}). However, based on the modest internal energy of CH_3 , the majority of this diagonal axis is due to translational energy (80%–85%). One striking feature of this triangle plot is the overwhelming fraction of reaction exothermicity being funneled into HF vibration and translational recoil. The plot is similar to the triangle plot for $\text{F} + \text{H}_2$,⁴¹ but with even slightly narrower rotational distributions. Such behavior is of course consistent with the dynamics for reactions on an early barrier potential energy surface.

In light of our previous study of nonadiabatic effects in the $\text{F} + \text{H}_2$ reaction,⁸ one interesting question is the potential importance of spin orbit excited $\text{F}^*(^2P_{1/2})$ present in the discharge F atom source. This is greatly aided by recent high-resolution photoelectron experiments, which have determined the bond dissociation energy^{42,43} for methane to be $36\,174(9)\text{ cm}^{-1}$. In conjunction with the well characterized HF bond dissociation energy^{44,45} of $47\,311(5)\text{ cm}^{-1}$, this predicts an overall reaction exothermicity of $\Delta H = 11\,137(10)\text{ cm}^{-1}$ or $31.84(3)\text{ kcal/mol}$, for the ground spin-orbit state of $\text{F}(^2P_{3/2})$ and the A -modification of methane ($J=0$). The total energy to be distributed into the products is $\Delta H + E_{\text{COM}} = 11\,767(210)\text{ cm}^{-1}$, where the energy uncertainty is now completely dominated by the angular distribution of collision geometries. It is worth noting that this

upper limit already presumes no internal energy in the CH_3 product, which provides an even tighter energetic constraint. This would predict that product states up to $\text{HF}(v=3, J=5)$ and $\text{HF}(v=2, J=14)$ could be energetically populated, which can be compared with populations experimentally observed up to $\text{HF}(v=3, J=5)$ and $\text{HF}(v=2, J=11)$ in the $v=3$ and 2 manifolds, respectively. At the 1σ uncertainty level we also observe extremely weak signals in $\text{HF}(v=3, J=6)$, which could be made energetically accessible by nonadiabatic reactions with spin-orbit excited F atoms ($\Delta E_{\text{spin-orbit}} = 1.15\text{ kcal/mol}$). Experiments on the $v=3$ manifold could in principle be used to interrogate possible non-adiabatic aspects of the reaction,⁸ but would first require further efforts to reduce the collision energy uncertainty.

The observed vibrational populations agree well with the theoretical predictions²⁰ of Corchado and Espinosa-Garcia. They found that the HF stretching motion is strongly coupled with the reaction coordinate in the exit channel, allowing vibrational excitation of the HF product. They also find that the CH_3 bending mode is coupled weakly to the reaction coordinate in the exit channel, and therefore little vibrational excitation in CH_3 is predicted. These results are consistent with the fact that reaction proceeds via an early barrier where the HF distance (1.360 \AA) (Ref. 20) is quite extended, 48% longer than the equilibrium HF bond length ($r_e = 0.9168\text{ \AA}$).^{21,32} In contrast, the CH distance (1.152 \AA) (Ref. 20) is only slightly extended (5%) over the CH_4 bond length ($r_0 = 1.094\text{ \AA}$).⁴⁶ The HF distance in the transition state falls between the $v=4$ and $v=5$ classical turning points²¹ in isolated HF, which corresponds to highly vibrationally excited HF product. The hot rotational distributions are consistent with a bent transition state, where the H receives recoil impulse from the CH_3 group in the exit channel due to H–C repulsion in the products. Indeed, as noted above, rotational states in $\text{HF}(v=2,3)$ are populated up to or near the energetic limit. Furthermore, the $\text{HF}(v=1)$ rotational distribution is very broad (Fig. 8), with population observed up to the highest J levels probed.

We have performed a simple Franck–Condon analysis of the transition state geometry in order to gain further insight into the reaction dynamics. Our analysis consists of evaluating one-dimensional overlap integrals between asymptotic vibrational wave functions (for both HF and CH_3 product molecules) and the *ab initio* transition state²⁰ geometry, where we focus on the HF stretch and CH bend manifolds. Numerically converged eigenvalues and wave functions are calculated in a distributed Gaussian basis.⁴⁷ HF wave functions were calculated using a simple Morse potential;²¹ the distribution of initial transition state geometries is characterized by a Gaussian distribution (centered at $r_{\text{H-F}} = 1.360\text{ \AA}$) (Ref. 20) with a width of 0.25 \AA (based on zero point amplitudes). The overlap integrals predict HF vibrational populations to increase rapidly with v , in good qualitative agreement with the observation for $\text{HF}(v=0-3)$. From a Franck–Condon perspective, this would require a rapidly changing C–H bond character at the transition state that results in vibrationally excited HF products. Similar studies of the CH_3 fragment^{48,49} have been explored for a Gaussian distribution of out of plane bending geom-

etries centered at the transition state geometry ($\angle_{\text{H-C-H}'} = 107.2^\circ$),²⁰ with a width of 12° . This Franck-Condon analysis predicts significant excitation of CH_3 bending modes, which is not consistent with the previous experimental results by Sugawara.³⁸ This behavior suggests that the relaxation of the CH_3 bend potential from methane (tetrahedral) to methyl radical (planar) occurs over a longer range of nuclear motion than HF formation and motion out the product channel. Indeed, this is qualitatively consistent with *ab initio* calculations,²⁰ which predict a relatively slow change in the CH_3 bending frequency along the reaction coordinate.

VI. CONCLUSIONS

Nascent rovibrational HF product state distributions have been obtained for the $\text{F} + \text{CH}_4 \rightarrow \text{HF}(v, J) + \text{CH}_3$ reaction, using direct infrared absorption detection in a crossed supersonic jets apparatus. Sub-Doppler resolution (0.0001 cm^{-1}) of the probe laser has revealed Doppler profiles with state specific structure with contributions from both absorption and stimulated emission. Integration of the absorption profiles yields column-integrated densities of HF molecules, which are then used to obtain scattered product HF populations by density-to-flux transformation. $\text{HF}(v=0)$ populations are probed directly, which permits nascent populations for all $\text{HF}(v=0,1,2,3)$ vibrational levels to be reported for the first time. The observed population of highly vibrationally excited HF product agrees well with *ab initio* potential surface predictions of an early reaction barrier. Furthermore, rotational states are observed in populations near the energetic limit for $v=2$ and $v=3$, with a very wide distribution for $v=1$, i.e., consistent with a bent transition state. The current work provides some of the most detailed quantum state-to-state results for a basic H-atom abstraction atom+polyatom systems. It is our hope that this will provide an incentive for further efforts in both the development of high quality *ab initio* potential surfaces as well as methods for addressing the quantum dynamics of chemical reactions in more complicated systems.

ACKNOWLEDGMENTS

This research has been funded by the Air Force Office of Scientific Research, with support from the National Science Foundation in the development of the pulsed slit discharge sources. W.W.H. thanks the National Research Council for a postdoctoral research fellowship.

¹W. B. Chapman, B. W. Blackmon, S. Nizkorodov, and D. J. Nesbitt, *J. Chem. Phys.* **109**, 9306 (1998).

²W. B. Chapman, B. W. Blackmon, and D. J. Nesbitt, *J. Chem. Phys.* **107**, 8193 (1997).

³M. Baer, M. Faubel, B. Martinez-Haya, L. Y. Rusin, U. Tappe, and J. P. Toennies, *J. Chem. Phys.* **108**, 9694 (1998).

⁴D. M. Neumark, A. M. Wodtke, G. N. Robinson, C. C. Hayden, and Y. T. Lee, *J. Chem. Phys.* **82**, 3045 (1985).

⁵G. Dharmasena, K. Copeland, J. H. Young, R. A. Lasell, T. R. Phillips, G. A. Parker, and M. Keil, *J. Phys. Chem. A* **101**, 6429 (1997).

⁶G. Dharmasena, T. R. Phillips, K. N. Shokhrev, G. A. Parker, and M. Keil, *J. Chem. Phys.* **106**, 9950 (1997).

⁷M. Faubel, L. Rusin, S. Schlemmer, F. Sondermann, U. Tappe, and J. P. Toennies, *J. Chem. Phys.* **101**, 2106 (1994).

⁸S. A. Nizkorodov, W. W. Harper, W. B. Chapman, B. W. Blackmon, and D. J. Nesbitt, *J. Chem. Phys.* **111**, 8404 (1999).

⁹J. F. Castillo, D. E. Manolopoulos, K. Stark, and H. J. Werner, *J. Chem. Phys.* **104**, 6531 (1996).

¹⁰M. H. Alexander, H. J. Werner, and D. E. Manolopoulos, *J. Chem. Phys.* **109**, 5710 (1998).

¹¹F. J. Aoiz, L. Banares, B. Martinez-Haya, J. F. Castillo, D. E. Manolopoulos, K. Stark, and H. J. Werner, *J. Phys. Chem. A* **101**, 6403 (1997).

¹²J. C. Corchado and H. J. Werner, *J. Chem. Phys.* **104**, 6515 (1996).

¹³E. Rosenman, S. Hochman-Kowal, A. Persky, and M. Baer, *Chem. Phys. Lett.* **257**, 421 (1996).

¹⁴D. E. Manolopoulos, *J. Chem. Soc., Faraday Trans.* **93**, 673 (1997).

¹⁵A. Gauss, Jr., *J. Chem. Phys.* **65**, 4365 (1976).

¹⁶J. C. Corchado and J. Espinosa-Garcia, *J. Chem. Phys.* **105**, 3160 (1996).

¹⁷H. Kornweitz, A. Persky, and R. D. Levine, *Chem. Phys. Lett.* **289**, 125 (1998).

¹⁸M. J. T. Jordan and R. G. Gilbert, *J. Chem. Phys.* **102**, 5669 (1995).

¹⁹T. Joseph, R. Steckler, and D. G. Truhlar, *J. Chem. Phys.* **87**, 7036 (1987).

²⁰J. C. Corchado and J. Espinosa-Garcia, *J. Chem. Phys.* **105**, 3152 (1996).

²¹J. A. Coxon and P. G. Hajigeorgiou, *J. Mol. Spectrosc.* **142**, 254 (1990).

²²M. A. Nazar and J. C. Polanyi, *Chem. Phys.* **55**, 299 (1981).

²³M. A. Wickramaaratchi, D. W. Setser, H. Hildebrandt, B. Korbitzer, and H. Heydtmann, *Chem. Phys.* **94**, 109 (1985).

²⁴M. Maneshkarimi and H. Heydtmann, *Chem. Phys. Lett.* **234**, 182 (1995).

²⁵D. J. Bogan and D. W. Setser, *J. Chem. Phys.* **64**, 586 (1976).

²⁶W. H. Duewer and D. W. Setser, *J. Chem. Phys.* **58**, 2310 (1973).

²⁷K. C. Kim and D. W. Setser, *J. Phys. Chem.* **77**, 2493 (1973).

²⁸S. Davis, D. T. Anderson, G. Duxbury, and D. J. Nesbitt, *J. Chem. Phys.* **107**, 5661 (1997).

²⁹D. Proch and T. Trickl, *Rev. Sci. Instrum.* **60**, 713 (1989).

³⁰D. D. Nelson, Jr., A. Schiffman, K. R. Lykke, and D. J. Nesbitt, *Chem. Phys. Lett.* **153**, 105 (1988).

³¹D. Kaur, A. M. Souza, J. Wanna, S. A. Hammad, L. Mercorelli, and D. S. Perry, *Appl. Opt.* **29**, 119 (1990).

³²R. S. Ram, Z. Morbi, B. Guo, K. Q. Zhang, P. F. Bernath, J. Vander Auwera, J. W. C. Johns, and S. P. Davis, *Astrophys. J.* **103**, 247 (1996).

³³J. L. Hall and S. A. Lee, *Appl. Phys. Lett.* **29**, 367 (1976).

³⁴A. Persky, *J. Phys. Chem.* **100**, 689 (1996).

³⁵W. W. Harper, S. A. Nizkorodov, and D. J. Nesbitt (unpublished).

³⁶E. Arunan, D. W. Setser, and J. F. Ogilvie, *J. Chem. Phys.* **97**, 1734 (1992).

³⁷W. T. Zemke, W. C. Stwalley, S. R. Langhoff, G. L. Valderrama, and M. J. Berry, *J. Chem. Phys.* **95**, 7846 (1991).

³⁸K. Sugawara, F. Ito, T. Nakanaga, H. Takeo, and C. Matsumura, *J. Chem. Phys.* **92**, 5328 (1990).

³⁹D. J. Bogan and D. W. Setser, *J. Chem. Phys.* **64**, 586 (1976).

⁴⁰M. Gonzalez (private communication).

⁴¹J. C. Ploanyi and K. B. Woodall, *J. Chem. Phys.* **57**, 1574 (1972).

⁴²K.-M. Weitzel, M. Malow, G. K. Jarvis, T. Baer, Y. Song, and C. Y. Ng, *J. Chem. Phys.* **111**, 8267 (1999).

⁴³J. A. Blush, P. Chen, R. T. Wiedmann, and M. G. White, *J. Chem. Phys.* **98**, 3557 (1993).

⁴⁴W. C. Stwalley, *Chem. Phys. Lett.* **6**, 241 (1970).

⁴⁵W. T. Zemke, W. C. Stwalley, J. A. Coxon, and P. G. Hajigeorgiou, *Chem. Phys. Lett.* **177**, 412 (1991).

⁴⁶M. Dang-Nhu, A. S. Pine, and A. G. Robiette, *J. Mol. Spectrosc.* **77**, 57 (1979).

⁴⁷I. P. Hamilton and J. C. Light, *J. Chem. Phys.* **84**, 306 (1986).

⁴⁸T. J. Sears, J. M. Frye, V. Spirko, and W. P. Kraemer, *J. Chem. Phys.* **90**, 2125 (1989).

⁴⁹V. Spirko and P. R. Bunker, *J. Mol. Spectrosc.* **95**, 381 (1982).